Denis Bolshukhin, Rudolf Neu, Dieter Schlögl, Ralph Dux, Uwe Schumacher and ASDEX Upgrade Team

Measurement of Spurious Impurity Concentrations in ASDEX

Upgrade by X-Ray Spectroscopy

Denis Bolshukhin, Rudolf Neu, Dieter Schlögl, Ralph Dux, Uwe Schumacher and ASDEX Upgrade Team

Measurement of Spurious Impurity Concentrations in ASDEX Upgrade by X-Ray Spectroscopy

Measurement of spurious impurity concentrations in ASDEX Upgrade by X-ray spectroscopy

D. Bolshukhin, R. Neu, D. Schlögl, R. Dux, U. Schumacher and ASDEX Upgrade Team

Max-Planck-Institut für Plasmaphysik, EURATOM Association, Boltzmannstr. 2, D − 85748 Garching, Germany

Abstract. A two channel multi crystal spectrometer of Bragg geometry was used for measurements of absolute photon fluxes of ASDEX Upgrade plasmas in the wavelength range from 0.5 Å up to 26 Å. The calibration of the spectrometerwas was done by an *ab initio* calculation using the absolute reflection data from literature of 4 crystals. The calibration was validated by direct comparison with other absolute calibrated diagnostics at the ASDEX Upgrade as well as by using the impurity transport code STRAHL. The absolute impurity concentrations of elements from N up to Cu have been extracted. O and F appear to be main impurity components after C, which is routinely measured by independent diagnostic. Other impurities either have never been seen or (like Fe and Cu) appear only sporadically and normally do not contribute significantly to plasma radiation in soft x-ray range.

Short title: Impurity concentrations in ASDEX Upgrade

April 5, 2000

2

1. Introduction

Although impurity concentrations in tokamak plasmas have been strongly reduced by introduction of the divertor concept and wall conditioning [1, 2], the strong limits imposed by a future fusion device [3] still justify strong efforts for the detection and the control of impurities. Since medium-Z or high-Z materials as tungsten may be used as plasma facing components in ITER [4] or a comparable device, X-ray spectroscopy is of special interest since it is the most sensitive and element specific diagnostic in the main plasma for impurities with charge numbers above $Z > 18$. (Only recently a quantitative diagnostic by charge exchange spectroscopy was developed for Ar ($Z = 18$)[5, 1]). Additionally, there is a growing interest in plasma discharges with internal transport barrier. This barrier might cause enhanced central impurity concentrations and therefore the central diagnostic of such plasmas is of great importance.

At ASDEX Upgrade there are several X-ray diagnostics in use. The soft x-ray diagnostic (SXR) [6] uses the array of the x-ray sensitive diodes placed inside pin-hole cameras with the various filter foils for the variation of the low energy threshold for measuring the whole x-rays. Although having a high sensitivity, and a very high temporal resolution the SXR diagnostic is indeed not suited to identify the impurities which contribute to the total radiation. A wavelength selective impurity diagnostic in the soft X-ray region is the so called carbon oxygen monitor (COM) [7]. Under the normal discharge conditions C and O are the main impurities in ASDEX Upgrade. Therefore the COM is designed as a two channel Bragg crystal monochromator for the observation of the Lyman-α line emission of OVIII and CVI only. A high resolution Johann spectrometer is also available at ASDEX Upgrade. Originally it was designed to measure the ion temperature from the Doppler broadening of spectral lines from He-like chlorine or argon, but in principle it can cover the wavelength range from 1.1 Å up to about 19 Å. In practice however only a very small wavelength range must be selected, since no interchange of the reflecting crystal is possible without braking the spectrometer vacuum.

However, in order to get a flexible and broad band impurity diagnostic in the X-ray region an additional, multi purpose spectrometer is necessary. At ASDEX Upgrade a two channel rotating crystal Bragg spectrometer is in use since 1994. Unlike the paper of N.J. Peacock et al. [1], where particularly the calibration a similar spectrometer at the JET tokamak is described, this paper additionally will give a detailed technical insight in the spectrometer as well as the results of a systematic investigation on the identification as well as the quantification of the most prominent impurities in ASDEX Upgrade.

In the next section the experimental setup of the Bragg crystal spectrometer will be described whereas in Section 3 the procedure of the absolute calibration is presented.

Finally in Sec. 4 the results of the systematic impurity investigations will be discussed.

2. Experimental setup of the Bragg crystal spectrometer

A Bragg crystal spectrometer makes use of the Bragg reflection, i.e. the reflection of collimated X-rays incident on a flat crystal with layer spacing d. X-rays with wavelength λ are only reflected, if the glancing angle ϑ fulfills the Bragg equation

$$n \cdot \lambda = 2d \cdot \sin \vartheta \qquad (1)$$

with n being the reflection order. Incoming x-rays from an angle of ϑ are reflected by a crystal into an angle of 2ϑ if the Bragg condition is fulfilled. In case of the scanning mode both, crystal and detector are rotated simultaneously with angular velocities ω and 2ω during a plasma discharge to measure a spectrum. This implies that not a whole spectrum, but only one wavelength at any point of time can be observed. In the monitoring mode crystal and detector are kept fixed under angles ϑ and 2ϑ to measure the temporal evolution of the at a constant wavelenght.
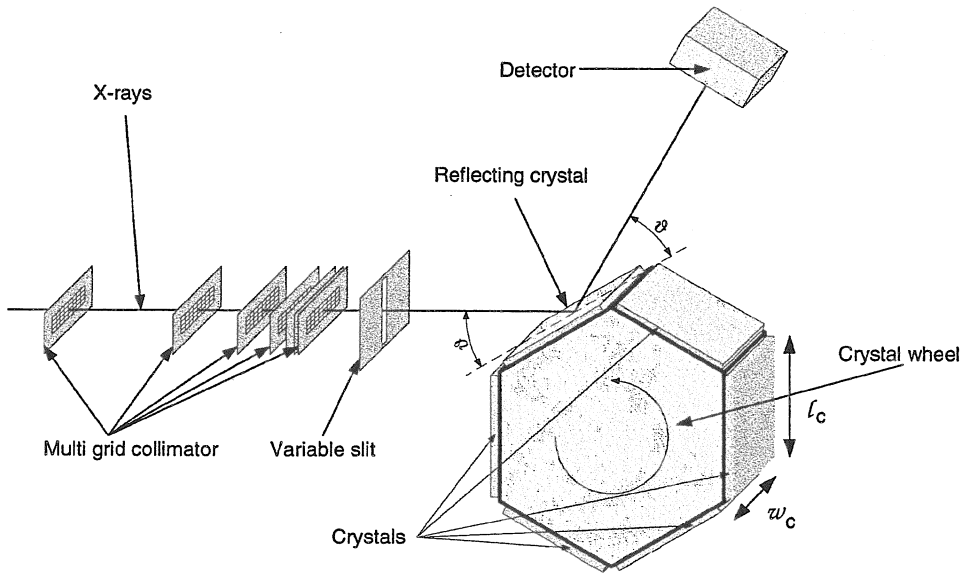

Figure 1. Experimental setup of one Bragg crystal spectrometer at ASDEX Upgrade. X-rays emitted from the plasma enter the spectrometer from the left.

At ASDEX Upgrade two similar Bragg crystal spectrometers exist, which are placed in a common vacuum vessel. The spectrometers, the premplifiers and the power supplies and are situated in a large concrete housing for shielding from neutron and gamma radiation. In this paper they are referred to as "system A" and "system B". The schematic

setup of system A is shown in figure 1. X-rays emitted from the plasma first pass a multigrid collimator [8] and an entrance slit 40 mm high and 0 – 50 mm wide. It allows the necessary reduction of incoming photon fluxes. For detection a Multi Strip Gaseous Chamber (MSGC) is used [9, 10], which performs single photon counting with count rates above 1 MHz [7]. The crystal is fixed on a crystal revolver which allows a selection of 1 crystal out of 6 without breaking the vacuum between two subsequent discharges. Both systems, A and B, observe the plasma in radial direction along a horizontal line of sight 14 cm above the mid plane which crosses almost the center of the plasma. The toroidal distance between the lines of sight of system A and B is only 9 cm. The only dissimilarity between system A and B is a different set of crystals mounted in each system (see table 1) and a slightly different setup of the collimator, which will be discussed below.

2.1. Multi grid collimator

The multi grid collimator performs the one dimensional collimation of the incoming x-rays. It consists of 7 (system A) or 6 (system B) consecutively mounted similar brass sheets, each with an aperture 59.8 mm wide and 29.95 mm high. 11 vertical and 54 horizontal bars with widths of 0.3 mm divide the apertures in a two dimensional array of 4.8 mm wide and 0.25 mm ($= d_y$) high collimating holes. With their thicknesses of 150 μm the brass sheets are opaque for X-rays below 15 keV (≥ 0.8 Å). Distances between the grids are optimized in a way, that X-rays with too high divergence angles hit one of the bars which form the collimating holes [11]. This condition is fulfilled if the distance between the next grid pair is approximately twice the distance between the previous one (see Fig.1). Therefore only those X-rays pass the collimator which pass all grids through the similar hole and the maximimum possible divergence angle α_{max} is given by

$$\alpha_{max} = \arctan\left(\frac{d_y}{L}\right) \qquad (2)$$

with d_y being the height of the holes and L the distance between first and last brass sheet. With the total collimator lengths $L_A = 458.7$ mm and $L_B = 225.7$ mm for systems A and B the maximum possible divergence angle in vertical direction are $\alpha_{max,A} = \pm 0.55$ mrad and $\alpha_{max,B} = \pm 1.11$ mrad, respectively. The collimation of system B has been reduced to facilitate the observation of one spectral line in the Monitoring Mode. The experimentally determined collimator transmission has nearly the theoretically predicted dependence on angle near 0°. The collimator shows a few narrow transmission windows at angles different to 0°, yet with rather low transmission. They can occur due to the limitation of the grid precision and the precision of the

holding frame as well. Effects caused by the side transmission bands of the collimators will be discussed in section 2.3.

2.2. MSGC detector

The multi strip gaseous chamber (MSGC) has an optimum geometry in association with its high response to x-ray photons. It follows the design first proposed by A. Oed [9]. Thin gold strips (8 μm), called anode strips, are evaporated onto a glass substrate. Between each pair of them another broader gold strip (150 μm) is evaporated, a so-called cathode strip. This glass substrate is mounted into a volume with a continiously flow of argon counting gas. The counting gas exhaust is directly connected to the atmosphere. This insures the pressure inside the chamber to be equal to atmospheric pressure. 9 mm above the glass plate the volume is terminated by a 2 μm thick Mylar† foil covered by a 80 nm thick aluminum layer. The construction of the detector was described in detail in [7]. It differs to the latter only by operational amplifiers used in the electronic, yielding a better linearity at high photon fluxes and a shorter dead time. The sequence of anode and cathode strips forms the sensitive area of the detector of $30 \cdot 40$ mm^2. The dimensions of the detector were optimized to registrate all the reflected photons: also in the case of the small excursions of the detector from its optimal position due to a limited precision of the spectrometer mechanics and the stepping motor. The geometry of the detector was optimized in such a way, that the light bundle passing the completely opened entrance slit (40 mm) being reflected by crystal at 80° covers the full detector width at the angle of 160°. The depth of the detector volume of 9 mm is optimized to insure a complete stopping of photons in the used energy range by the counting gas, but simultaneously to minimize the absoption of high energy photons with energies above 15 keV, which are not stopped by the collimator material and are responsible for the background signal. The transmission of the aluminium covered mylar window sets the low detector threshold to 150 eV.

A second MSGC, which is completely enclosed by the thick metallic housing is directly mounted on the backside of the x-ray detecting MSGC. It has same dimensions and electronics and yields the background countrate due to neutron induced gamma radiation. During plasma discharges with high neutron rate and closed spectrometer entrance the measured countrates of two detectors had a ration of 1/1.5. By subtraction of this calibrated background signal the correction of the spectra was performed.

---

† Mylar = Polyethylenterephtalate

6

2.3. Crystals

For each system 6 crystals are available on the crystal wheel. Each crystal is $l_c = 100$ mm long and $w_c = 50$ mm wide and can be selected before a plasma discharge. During the plasma discharge the crystal revolver is kept fixed. The wavelength range for any single crystal is limited with the upper limit of $2d$ due to the Bragg condition Eq. 1. In general the lower limit of the measurement is restricted due to the UV light reflection at small glancing angles to about 1/10 of double crystal spacing $2d$ [12]. At about 9° light through the side transmission bands of the collimator and at 7.5° light from the main transmission band of the collimator directly reaches the detector (see figure 2). This causes a strong increase of the signal seen by measurements at the lower wavelength limit of the spectrometer. In table 1 all available crystals are listed together
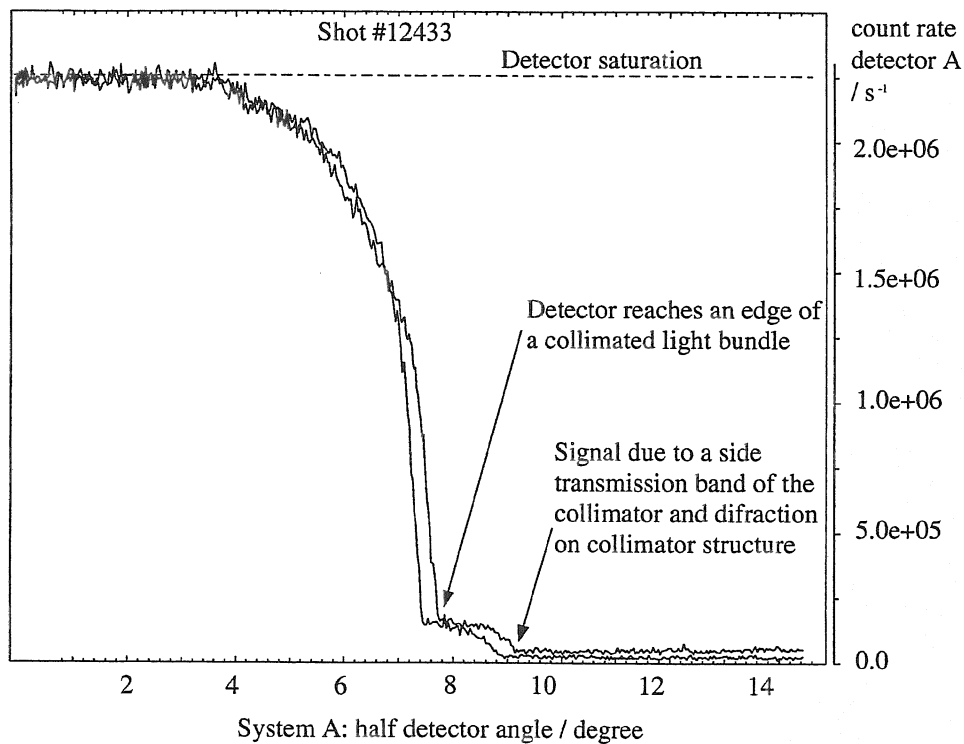

Figure 2. The count rate of detector A as a function of the half detector angle during plasma discharge when crystal angle is kept at 0°. The count rate rises slightly at 9.2° due to scattered and diffracted light and then rises sharply as the detector enters a collimated light bundle at 7.5°. The positions of the edges are slightly different in forward and return scan of the detector angle due to a hysteresis of the spectrometer mechanics.

with their wavelength range, for usable crystal angles ranging from 9° to 80°. They cover the whole wavelength range between 0.47 Å and 100.0 Å.

Nr.	System A			System B		
	Crystal	$2d$ [Å]	measurement range [Å]	Crystal	$2d$ [Å]	measurement range [Å]
1	Topaz (303)	2.712	0.47 - 2.70	Topaz (303)	2.712	0.47 - 2.70
2	Silicon (111)	6.271	1.09 - 6.25	Silicon (111)	6.271	1.09 - 6.25
3	ADP (101)	10.640	1.85 - 10.61	ADP (101)	10.640	1.85 - 10.61
4	KAP (100)	26.579	4.60 - 26.47	KAP (100)	26.579	4.60 - 26.47
5	Lead stearate	100.4	17.0 - 100.0	Lead stearate	100.4	17.0 - 100.0
6	Multilayer	96.5	16.8 - 96.1	LiF (220)	2.848	0.47 - 2.80

Table 1. Available crystals for both Bragg crystal spectrometers at ASDEX Upgrade. The wavelength range for all crystals is given for Bragg angles between 9° and 80°. Measurements at the angles above 80° are not useful because of partial shadowing of the crystal by the detector.

The necessary reflection data for different crystals have been used for the absolute calibration of the spectrometer. The integral reflection curve of ADP (101) (see Fig. 3) is available from the literature [21], the Si (111) and LiF (220) were calculated point by point with the GID computer code [22]. The calibration functions of these new introduced crystals were compared with the absolute calibrated KAP crystal. In the cases of the Si crystal and the ADP crystal a direct comparison of the simultaneously measured with the KAP crystal brightnesses of He-like lines of silicon was possible.

The absolute calibration for the LiF (220) crystal was checked by a more indirect method. Using the transport code STRAHL [23] the calculated emissivities of Ne- and He-like Fe transitions for the same plasma discharge were compared with measured ones. In the case of the He-like Fe measurements were done with the LiF (220) and the Ne-like Fe was measured with KAP crystal. For the calculation of the iron emissivities the atomic data from [24] for He-like ions and from [25] for Ne-like ions were used. After the introduction of a correction factor for the LiF crystal the theoretical and experimental emissivities of Fe in different plasma discharges determined from Ne- and He-like Fe ion species agree within a factor of two. The discrepancy can be accounted by the variation of the Fe signals during the plasma discharge. As a result of this procedure absolute measurements between 0.5 Å and 26 Å become possible.

In the scanning mode a crystal is rotated with an angular velocity of up to $\omega = 16.7$ °/s. This results in one full spectrum during 4 s ($\approx$ 2 spectra per discharge). When scanning portions of the whole spectrum, several scans per discharge are pos-
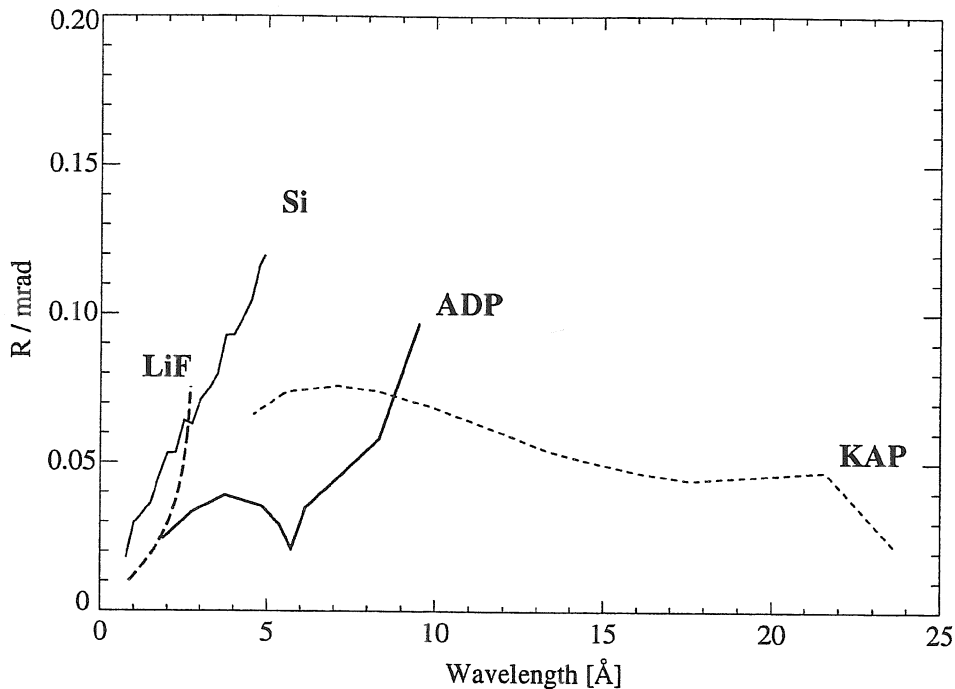
8

Figure 3. Integral reflection curves of LiF - thick dashed line, Si - thin solid line, ADP - thick solid line and KAP - thin dashed line.

sible. The time resolution of the spectrometer is determined by the sampling rate of the aquisition system, which can be set up to 10 kHz. For sufficient counting statistics a sampling rate of 1 kHz is used leading to about 6 data points per *fwhm*, which is adequate for spectroscopical applications.

2.4. Second order of reflection

Specular reflection in the second and higher orders corresponding to $n = 2, 3, ..., n$ in Eq.1 usually contains only a few percent of the incoming radiation flux. Thus, only strong spectral lines can be observed in second order.

Especially in situations, where the first order lines are strongly saturated it is advantageous to observe these lines in second order as is demonstrated in the follo;wing example of lines from H- and He-like silicon. The Si spectrum recorded in the first reflection order (upper part of Fig.4 picture) is strongly saturated causing a very broad line shape. Although the influence of the dead time on the count rates can be corrected according to the procedure described in section 3.1, the corrected count rates may have large uncertainties, if the raw signal is significantly saturated. The measured signals of

the strong spectral lines can of course be reduced using a smaller entrance slit, but this leads to too weak signals for spectral lines of moderate or low intensities. Therefore the second order reflection can be used for the strong lines instead (see lower part of Fig. 4). This allows simultaneous measurements of the strong and weak spectral lines in the non saturated detector regime. Furthermore, the Si lines in the spectrum in the second order of reflection are better resolved due to by a factor two smaller angular dispersion by similar line width as compared to spectrum of first order of reflection (see lower part of Fig. 4). The angular dispersion can be obtained differentiating the relation 1 with respect to ϑ. It should be kept in mind, that for the measurements of absolute line intensities with spectra of the second order of reflection an integral reflectivity in the second order and a wavelength correction have to be introduced into the calibration function (see section 3), while the detector's is just a function of photon energy.

3. Absolute calibration of the spectrometer

3.1. Dead time correction

In figure 5 (a) a spectrum is shown which displays, among other lines the Lyman series of neon after the injection of neon doped pellets. In contrast to the spectrum shown in figure 5 (b) the maximum count rate of transitions $1s - np$ does not increase with decreasing n but stays approximatly constant for all $n < 5$. From this observation and also from the observation shown in Fig.2, it has been concluded, that the detector has a dead time τ of the non extended type. This means that increasing photon fluxes do not decrease the detector count rate. Following reference [14] the true event rate n_{real} and the measured count rate n_{meas} are related by

$$n_{\mathrm{meas}} = \frac{n_{\mathrm{real}}}{1 + n_{\mathrm{real}} \cdot \tau} \tag{3}$$

$$\Longleftrightarrow \quad n_{\mathrm{real}} = \frac{n_{\mathrm{meas}}}{1 - n_{\mathrm{meas}} \cdot \tau}. \tag{4}$$

Using equation 3 the maximum possible count rate n_{max} can be derived as

$$n_{\mathrm{max}} = \lim_{n_{\mathrm{real}} \to \infty} (n_{\mathrm{meas}}) = \frac{1}{\tau}. \tag{5}$$

The hereby derived value of τ for 3 different detector individuals which have been used in both systems A and B of the Bragg spectrometer are shown in table 2.

As it has been mentioned in [15] Eq. 3 fits the real measured signal just for moderate count rates, but not if the detector approaches saturation.

The dead time correction following Eq.3 becomes highly uncertain for $n_{meas} \to \frac{1}{\tau}$ [15]. Therefore countrates up to $n_{meas} < 80\%$ of $\frac{1}{\tau}$ can be dead time corrected
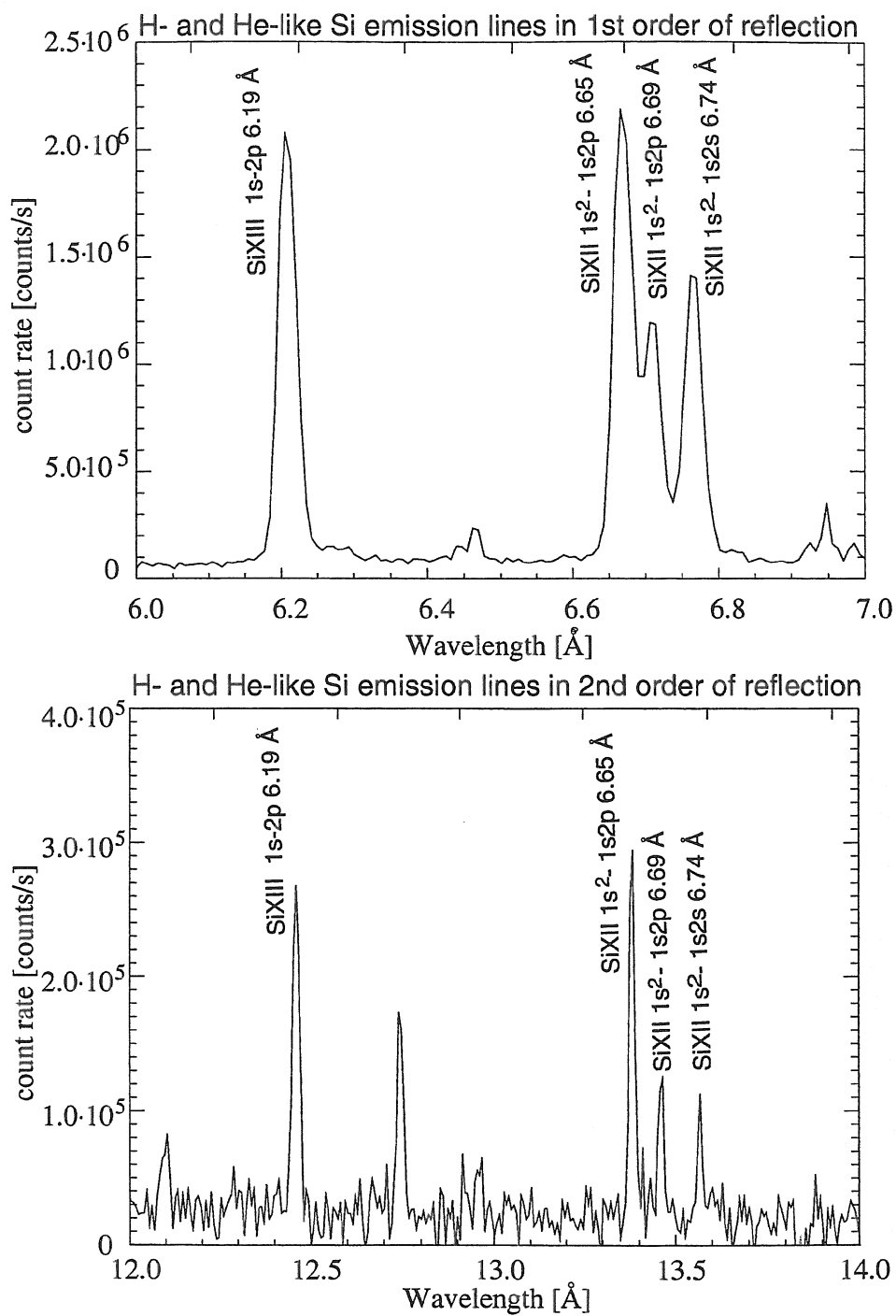
10

Figure 4. H- and He-like Si spectra measured in first (upper spectrum) and second (lower spectrum) order of reflection of the KAP crystal in discharge 12531.
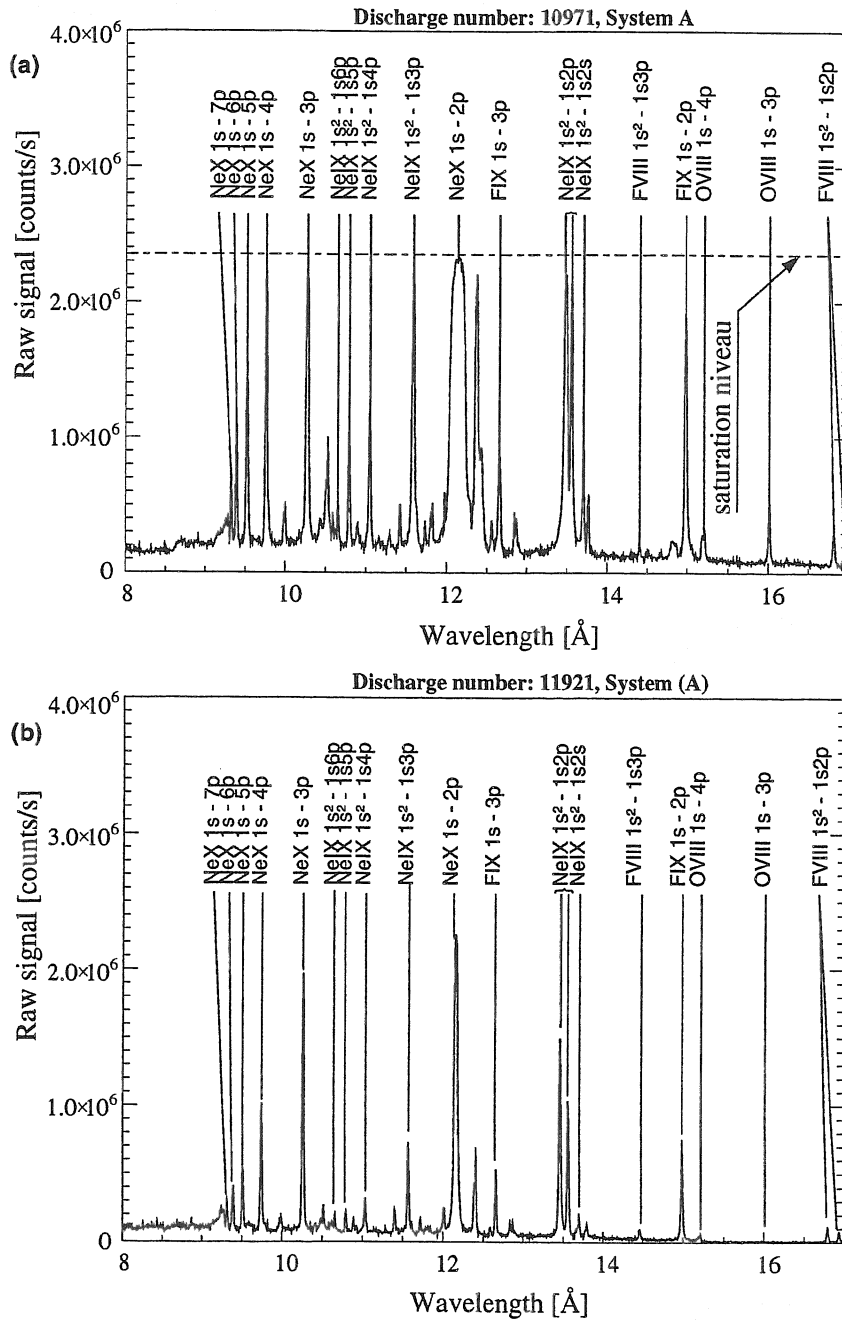
Figure 5. (a) Spectrum with very high count rates measured with detector number 2. The whole Lyman series of H- and He-like neon can be seen. For transitions $1s - np$ saturation occurs for quantum numbers $n < 5$. From the count rate measured in the peaks of the saturated lines dead times have been determined for the MSGC detectors. (b) Similar spectrum in the almost non saturated case except for $1s - 2p$ transition.
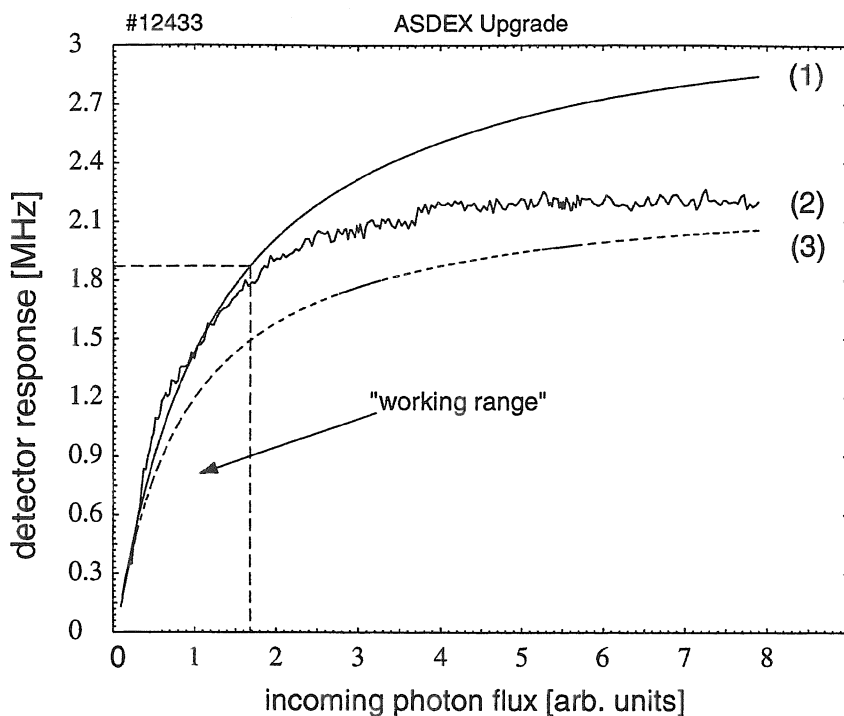
Figure 6. Some remarks on dead time correction: (1) – n_{meas} concerning to Eq.3 when $\tau = 300$ ns is applied; (2) – measured detector response on the linearly rising photon flux; (3) – n_{meas} when $\tau = 430$ ns is applied. The better fit of the working range of the detector is obtained for the dead time considerably smaller to that followed from the saturation signal of the detector.

without large uncertainties. The signals up to 80 % of the saturation level have been approximated with $\tau_{eff} = 300$ ns. This effective dead time is different to that directly obtained from saturation count rates (see Eq. 5). In Fig. 6 (2) detector response on the almost linearly rising photon flux onto the detector is shown. The resulting measurement curve has been approximated with the function shown in Eq.3 twice: (1) with $\tau_{eff} = 300$ ns (a practical approach), and (3) with $\tau = 430$ ns obtained from the saturation level. Since the τ_{eff} is optimised up to count rates of $1.8 \cdot 10^6 Hz$, count rates above this level were discarded.

3.2. Subtraction of detector background

The main source of background during a plasma discharge is a neutron induced gamma radiation, which is counted by the MSGC detectors. The corresponding count rates vary strongly throughout the discharge and reach up to 80 kHz during a high performance discharge in deuterium. The electronik noise and counts due to the other reasons can be neglected compared to gamma background. The background count rate of 80 kHz

Detector number	Maximum count rate n_{max} [MHz]	Dead time τ_{sat} [ns]	τ_{eff}[ns]
1	1.7	590	400
2	2.2	450	310
3	2.3	430	300

Table 2. Dead times of all three individual detectors used in the Bragg crystal spectrometer at ASDEX Upgrade. They have been derived from their maximum count rates by using equation 5 (τ_{sat}) and by using of linearly rising signals (τ_{eff}).

is about 5 % of the detector saturation level, therefore the dead time correction of background signals amounts just to 2 % which is below precision of the bqachground signal due to the statistic. Denoting n_{back} as the total measured background count rate and k as a calibration factor of the bachground channel, the true incident x-ray photon flux causes the count rate

$$n_{photon} = n_{real} - k \cdot n_{back}. \tag{6}$$

3.3. Detector efficiency

The detector efficiency is given by the absorption A_{gas} of the counting gas, reduced by the transmission T_{foil} through the foil covering the detecting volume:

$$\eta_{det} = A_{gas} \cdot T_{foil}. \tag{7}$$

The foil consists of a mylar substrate which is coated by an aluminum layer. The transmission T_{foil} is given by

$$T_{foil} = T_{mylar} \cdot T_{al} \qquad \text{with } T_{mylar} \text{ and } T_{al} \text{ calculated by} \tag{8}$$

$$T = e^{-\mu(\lambda) \cdot \rho \cdot d}. \tag{9}$$

Here d denotes the thickness and ρ the density of each layer. The mass absorption coefficient $\mu(\lambda)$ is a function of the photon wavelength and was taken from Henke et al. [16] and the internet publication of the National Institute of Standards and Technology [17]. According to the specification the nominal thickness of the mylar foil is $d_{mylar} = 2$ μm and its density $\rho_{mylar} = 1.38$ g/cm^3. In case of the evaporated aluminum layer the area density was measured during the coating process to be $\sigma_{al} = \rho_{al} \cdot d_{al} = 22$ μg/cm^2. As counting gas a mixture of Ar (83.25 %), methane (9.25 %) and butane (7.5 %) is used. The absorption of methane and butane for x-rays is much smaller than that of the argon gas and can therefore be neglected. Thus the absorption of the detector gas is given by the absorption of the argon gas which is given
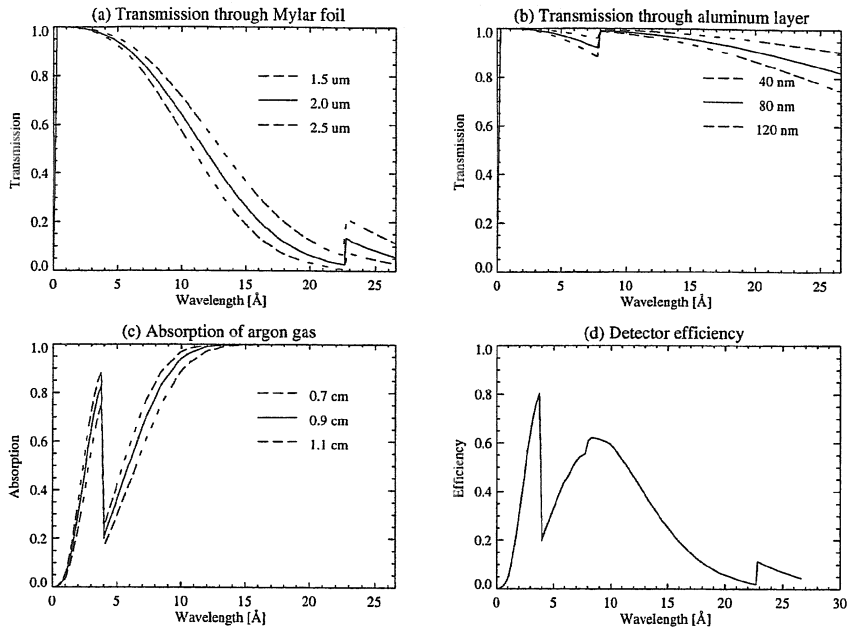
Figure 7. The detector efficiency and all contributing transmissions/absorptions are shown for nominal thicknesses of the layers and small variations. (a) Transmission through Mylar foil of thicknesses 1.5 μm, 2.0 μm and 2.5 μm. (b) Transmission through an aluminum layer of 40 nm, 80 nm, 120 nm. (c) Absorption of a layer of 0.7 cm, 0.9 cm and 1.1 cm argon.

(d) Detector efficiency for nominal thicknesses (2.0 μm Mylar, 80 nm aluminum and 0.9 cm argon).

by the formula

$$A_{\mathrm{Ar}} = 1 - e^{\mu_{\mathrm{Ar}}(\lambda) \cdot \rho_{\mathrm{Ar}} \cdot d_{\mathrm{Ar}}}. \tag{10}$$

The mass absorption coefficient $\mu_{\mathrm{Ar}}(\lambda)$ was also taken from references [16, 17]. The detector volume thickness: d_{Ar} is 0.9 cm. The argon density is given by the argon fraction $f_{\mathrm{Ar}} = 0.8325$ in the gas and the mean air pressure $p_{\mathrm{air}} = 0.954$ bar at 480 m above sea level, because the gas flow through the detector is open to atmosphere,

$$\rho_{\mathrm{Ar}} = \rho_{\mathrm{Ar},0} \cdot \frac{p_{\mathrm{air}}}{p_0} \cdot f_{\mathrm{Ar}} = 1.30 \times 10^{-3} \ \mathrm{g/cm^3} \tag{11}$$

with the argon density $\rho_{\mathrm{Ar},0} = 1.66 \times 10^{-3}$ g/cm^3 at normal pressure $p_0 = 1.013$ bar. Variations of p_{air} due to weather influences are usually less than 5 % and have therefore been neglected. In figure 7 the resulting detector efficiency together with the transmission of mylar foil, aluminium layer and argon absorption are shown. In case of the aluminum foil uncertainties in the thickness measurement up to 50 % result only in small variations of the transmission. Also the absorption of argon results only in small variations of the detector efficiency if reasonable uncertainties in the measurement

of the thickness of the gas volume of below 0.2 cm are assumed. But variations of the mylar thickness can result in a significant reduction of the detector efficiency, especially in the long wavelength region. Due to the fabrication process variations the thickness of each individual mylar foil varies up to ± 50 % . This corresponds to transmission variations up to a factor of 2.3 at the wavelength of about 22 Å. Thus an additional calibration check is necessary, which will be given in section 3.5.

3.4. Calibration function

In this section the calibration function, i.e. the function necessary to convert detector count rates into radiance of emission lines, will be derived. For this purpose an isotropically radiating source with radiance B_0 was considered. This assumption is consistent with real measurements at the ASDEX-Upgrade plasma. Further a wavelength distribution $f(\lambda)$ is assumed, which leads to a spectral radiance $\hat{B}(\lambda) = \tilde{B}_0 \cdot f(\lambda)$. Finally the spectral photon radiance is $B(\lambda) = \tilde{B}(\lambda)/(hc/\lambda)$.

Further we consider a fixed direction $\Omega(\alpha, \beta)$ with α denoting the same direction as the crystal rotation and β being the direction perpendicular to α, where $\alpha = \beta = 0$ is the direction along the spectrometer axis. The photon flux n_{det} into the detector of the spectrometer is determined by the detector efficiency $\eta_{\text{det}}(\lambda)$ as calculated in section 3.3, the collimator transmission $T_{\text{coll}}(\Omega)$, the reflection $R(\Omega, \theta, \lambda)$ of the crystal positioned at the angle θ (which is also called the "Prince function") and the cross section area $A(\Omega, \theta)$ of the light bundle that enters the detector aperture along the Ω-direction:

$$n_{\text{det}} = \int\limits_{\lambda=0}^{\infty} \int\limits_{\Omega} B(\lambda) \cdot \eta_{\text{det}}(\lambda) \cdot T_{\text{coll}}(\Omega) \cdot R(\Omega, \theta, \lambda) \cdot A(\Omega, \theta) \cdot d\Omega \cdot d\lambda. \quad (12)$$

The collimator transmission $T_{\text{coll}}(\Omega)$ is normalized in a way, that for the direction along the spectrometer axis it simply has the value of the shadowing by the horizontal and vertical bars of one collimator brass sheet:

$$T_{\text{coll}}(\Omega(0,0)) = \frac{A_{\text{coll}} - A_{\text{bars}}}{A_{\text{coll}}} \quad (13)$$

with A_{coll} = aperture of one brass sheet and A_{bars} = total area of all horizontal and vertical bars in one brass sheet. The effective collimation function $A(\Omega, \theta)$ of the detected light bundle is a function of the overlaps from collimator aperture, spectrometer slit aperture, crystal cross section at the crystal angle θ, and the detector aperture. When rotating the crystal from the initial angle θ_1 to the final angle θ_2 with constant angular velocity $\omega = d\theta/dt$ the total number of counts measured in the detector is given by

$$N_{\text{det}} = \int\limits_{\theta=\theta_1}^{\theta_2} \frac{n_{\text{det}}}{\omega} \cdot d\theta \quad (14)$$

Inserting equation 12 in equation 14 results in

$$
N_{\text{det}} = \frac{1}{\omega} \int_{\lambda=0}^{\infty} \int_{\theta=\theta_1}^{\theta_2} \int_{\Omega} B(\lambda) \cdot \eta_{\text{det}}(\lambda) \cdot
$$
$$
\cdot T_{\text{coll}}(\Omega) \cdot R(\Omega, \theta, \lambda) \cdot A(\Omega, \theta) \cdot d\Omega \cdot d\lambda \cdot d\theta =
$$
$$
= \frac{1}{\omega} \int_{\lambda=0}^{\infty} \int_{\Omega} B(\lambda) \cdot \eta_{\text{det}}(\lambda) \cdot T_{\text{coll}}(\Omega) \cdot
$$
$$
\cdot \left(\int_{\theta=\theta_1}^{\theta_2} R(\Omega, \theta, \lambda) \cdot A(\Omega, \theta) \cdot d\theta \right) \cdot d\Omega \cdot d\lambda \tag{15}
$$

As can be seen in figure 5, the wavelength range observed by the Bragg crystal spectrometer is dominated by line emission rather than continuum radiation. Thus the total spectral photon radiance $B(\lambda)$ can be written as the sum of individual spectral photon radiances $b_i(\lambda - \lambda_i)$ of each emission line i:

$$
B(\lambda) = \sum_i b_i(\lambda - \lambda_i) = \sum_i \frac{\tilde{b}_i}{hc/\lambda_i} \cdot f_i(\lambda - \lambda_i) \tag{16}
$$

with $\tilde{b}_i$ denoting the total spectral radiance of each line. To determine the radiances $\tilde{b}_i$ from measured data first a function $g_i(\theta - \theta_{\text{Bragg}}(\lambda_i))$ must be determined, which describes the detector counts as a function of the crystal angle, if only one spectral line i irradiates the spectrometer. As the natural line widths measured in ASDEX Upgrade are usually ≈ 0.002 Å and therefore smaller than the spectrometer resolution (≈ 0.03 Å at 19 Å measured with the KAP crystal) this function is the same for all lines for a given crystal. The normalization of g_i will be determined from the condition $\int g_i(\theta - \theta_{\text{Bragg}}(\lambda_i)) \cdot d\theta = 1$, thus the total number of detector counts G_i belonging to each spectral line i is obtained by fitting functions $G_i \cdot g_i(\theta - \theta_{\text{Bragg}}(\lambda_i))$ to the measured data. This is only true, if the line radiance shows no temporal variations. Although if only a small angular interval is used to fit the data, G_i represents the total number of counts that would be measured, if the crystal was rotated through the whole interval $[0, \pi/2]$. Thus if using G_i as the number of detector counts N_{det} belonging to one line integration limits $\theta_1 = 0$ and $\theta_2 = \pi/2$ must be inserted in equation 15.

The dependence of the effective collimation function $A(\Omega, \theta)$ from the crystal angle θ originates from the dependence of the projection of the crystal surface on a plain which is perpendicular to the spectrometer axis. The flatter the crystal position, the less radiation is reflected into the detector. But because the shape $f_i(\lambda - \lambda_i)$ of a spectral line is strongly peaked around the central wavelength λ_i or the Bragg angle $\theta_{\text{Bragg}}(\lambda_i)$, respectively, only a small angle interval $\Delta\theta$ around $\theta_{\text{Bragg}}(\lambda_i)$ contributes to the integration. Usually $\Delta\lambda$ is small enough (see above), that the crystal position

changes only slightly while scanning an emission line and therefore the θ dependency of A can be neglected:

$$A(\Omega, \theta) \longrightarrow A(\Omega, \theta_{\text{Bragg}}(\lambda_i)). \tag{17}$$

Thus the product $T_{\text{coll}}(\Omega) \cdot A(\Omega, \theta)$ can be splitted into the transmission function of the spectrometer $q(\Omega, \theta_{\text{Bragg}}(\lambda_i))$ and the normalised beam divergency profile $r(\Omega, \theta_{\text{Bragg}}(\lambda_i))$

$$T_{\text{coll}}(\Omega) \cdot A(\Omega, \theta_{\text{Bragg}}(\lambda_i)) = q(\Omega, \theta_{\text{Bragg}}(\lambda_i)) \cdot r(\Omega, \theta_{\text{Bragg}}(\lambda_i)) \tag{18}$$

with r being normalised for each Bragg angle as:

$$\int r(\Omega, \theta_{\text{Bragg}}(\lambda_i)) \cdot d\Omega = 1. \tag{19}$$

This leads to the equation for one spectral line:

$$G_i = \frac{1}{\omega} \int\limits_{\lambda=0}^{\infty} \int\limits_{\Omega} b_i(\lambda - \lambda_i) \cdot \eta_{\text{det}}(\lambda) \cdot q(\Omega, \theta_{\text{Bragg}}(\lambda_i)) \cdot$$
$$\cdot \left(\int\limits_{\theta=0}^{\pi/2} r(\Omega, \theta_{\text{Bragg}}(\lambda_i)) \cdot R(\Omega, \theta, \lambda) \cdot d\theta \right) \cdot d\Omega \cdot d\lambda. \tag{20}$$

For further transformations the definition of the Prins integral [18] $R_C(\lambda)$ can be used. It integrates the reflection of a flat crystal in case of polychromatic, but perfectly collimated irradiation:

$$R_C(\lambda) := \int\limits_{\theta=0}^{\pi/2} R(\Omega(0,0), \theta, \lambda) \cdot d\theta. \tag{21}$$

In [18] Evans has shown, that the value of the Prins integral does not change, if an arbitrary but normalized beamspread $r(\Omega)$ is introduced, i.e.

$$\int\limits_{\theta=0}^{\pi/2} r(\Omega) \cdot R(\Omega, \theta, \lambda) \cdot d\theta = \int\limits_{\theta=0}^{\pi/2} R(\Omega(0,0), \theta, \lambda) \cdot d\theta = R_C(\lambda) \tag{22}$$

$$\forall \quad r(\Omega) \quad \text{with} \quad \int r(\Omega) \cdot d\Omega = 1.$$

Because of this invariance $R_C(\lambda)$ is also called the reflection integral. Inserting equation 22 into equation 20 leads to

$$G_i = \frac{1}{\omega} \left(\int\limits_{\lambda=0}^{\infty} b_i(\lambda - \lambda_i) \cdot R_C(\lambda) \cdot \eta_{\text{det}}(\lambda) \cdot d\lambda \cdot \right) \cdot$$
$$\cdot \left(\int\limits_{\Omega} q(\Omega, \theta_{\text{Bragg}}(\lambda_i)) \cdot d\Omega \right). \tag{23}$$

18

Again, assuming only slow changing of the transmission function of the spectrometer during the scanning of a single spectral line the transmission of the spectrometer can be determined as follows

$$Q(\lambda_i) := \int\limits_{\Omega} q(\Omega, \theta_{\mathrm{Bragg}}(\lambda_i)) \cdot d\Omega. \tag{24}$$

This leads to

$$G_i = \frac{R_C(\lambda_i) \cdot \eta_{\mathrm{det}}(\lambda_i) \cdot Q(\lambda_i)}{\omega} \cdot \int\limits_{\lambda=0}^{\infty} b_i(\lambda - \lambda_i) \cdot d\lambda =$$

$$= \frac{R_C(\lambda_i) \cdot \eta_{\mathrm{det}}(\lambda_i) \cdot Q(\lambda_i)}{\omega} \cdot \frac{\tilde{b}_i}{hc/\lambda_i}. \tag{25}$$

Rearrangement of the above written equation results in the wanted conversion from the number of measured detector counts G_i belonging to one line and the total radiance $\tilde{b}_i$ of the line:

$$\tilde{b}_i = G_i \cdot C(\lambda_i) \qquad \text{with} \qquad C(\lambda_i) = \frac{hc}{\lambda_i} \cdot \frac{\omega}{R_C(\lambda_i) \cdot \eta_{\mathrm{det}}(\lambda_i) \cdot Q(\lambda_i)}. \tag{26}$$

In figure 8 the result of the calibration function $C(\lambda_i)$ is shown for different slit apertures of the spectrometer, which is not purely linear because of the complex geometrical arrangement of collimator and slit.

3.5. Experimental verification of the ab initio calibration

The above *ab initio* calibration function was checked by comparing absolute line intensities of the Bragg spectrometer with a Si(Li) semiconductor detector and with another Bragg spectrometer, so called Carbon-Oxigen Monitor (COM). The Si(Li) detector is mounted in the same ASDEX Upgrade flange as the Bragg spectrometer and has the same line of sight. A detailed description of the Si(Li) system is given in [19].

The absolute calibration of the Si(Li) detector was calculated using a Be foil and gold layer transmission as well as absorbtion data of a Si(Li) detector crystal. Properties of the collimator system and of electronic components were also taken into account. The Si(Li) detector has a very simple geometry compared to the Bragg spectrometer, which was kept constant during the whole measurement. No crystal reflection data are necessary for its calibration. Therefore the absolute calibration of a semiconductor detector should be rather precise. Hence the absolutely measured with Si(Li) detector choosen line intensities can be compared with the same line intensities measured with Bragg spectrometer. This comparison is shown in figure 9. Using the line radiation of
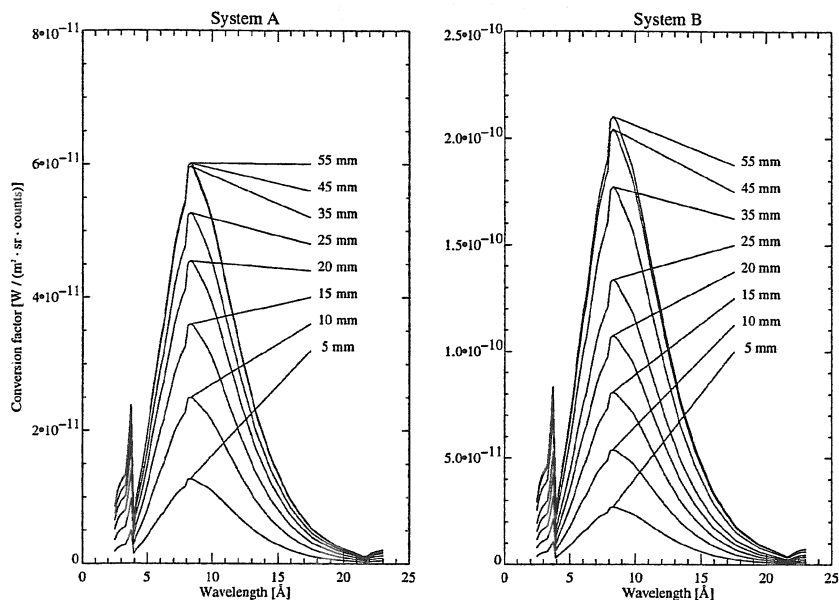
Figure 8. Calibration function used for the conversion of measured detector counts in line radiances for the KAP crystal. Due to different collimators both channel have different sensitivity which reflects in different y-scales for system A and B. The sensitivity of spectrometers rises first almost lineary with increasing of the slit width and than saturates after 45 mm, because the shadowed by the entrance slit range leave the cross section of the crystal/detector due to poor collimation in the direction perpendicular to the direction of the dispersion (x).

Ar at about 4 Å the verification of the absolute calibration of the Bragg spectrometer with help of Si(Li) detector, which will be discussed below, results in a correction factor of about 1.3 similar to that following from the comparison with the so called C-O monitor (see also figure 9). The line 1s – 2p of H-like oxygen at the wavelength of 18.97 Åwas selected. This wavelength is very close to the wavelength of maximum absorption around 22 Å and therefore small variations of the mylar thickness result in strong variations of the x-ray transmission. The line is continuously observed by the oxygen monitor, Bragg crystal monochromater at ASDEX Upgrade. In contrast to the Bragg crystal spectrometer discussed in this presentation the oxygen monitor possesses a KAP crystal which is fixed and continously observes the emission of the oxygen 1s – 2p line. This is comparable to the Monitoring Mode of the spectrometer discussed here. The oxygen monitor has been absolutely calibrated by means of an x-ray source [20]. A numerical simulation predicts the radiance to be a factor of $\gamma = 1.94$ higher for the oxygen monitor, where the line emission along a greater length is accumulated (see also sec. 4.2.
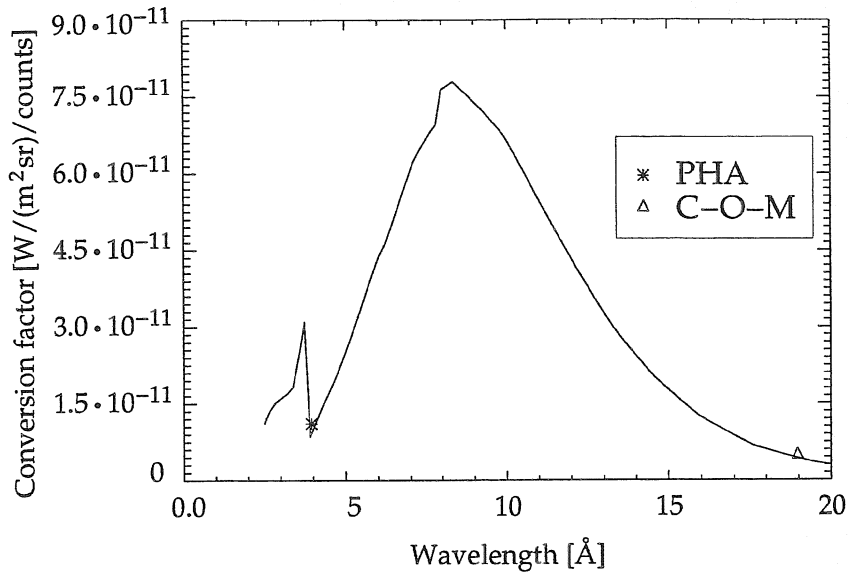
Figure 9. Calibration function of the Bragg spectrometer for entrance slit of 40 mm. Two data points give a comparison with other absolutely calibrated diagnostics. The star and the triangle are corresponding to the Si(Li) detector and to the C-O monitor respectively.

The rest dissimilarity of the conversion factors for two different diagnostics amounts just to the factor 1.3. It can be explained by suggestion of the deviation of the Mylar foil thickness from its nominal value, which will be discussed below. For further measurements of absolute emissivities with Bragg spectrometer the above discussed correction factor of 1.3 was introduced into the calibration function of the Bragg spectrometer. The disagreement could be partly explained by geometrical errors of foil thickness and detector volume thickness.

As has already been mentioned in section 3.3 the thickness of the Mylar foil covering the detector is specified with uncertainty up to $\approx$ 50 %, which results in a strong uncertainity of the Mylar transmission. This uncertainity can be eliminated with the use of equation 26 by measuring the radiance of an emission line simultaneously with the Bragg crystal spectrometer and another diagnostic. Comparison of both results in an "effective" Mylar thickness which can be used for all wavelength. When comparing both, C-O and Bragg spectrometers their different lines of sights have to be taken into account. While the spectrometer discussed here observes the mid plane of the ASDEX Upgrade plasma along a horizontal direction, the oxygen monitor observes along a vertical direction. The correction factor κ is can be calculated from the measured radiances $b_{oxygen,a}$ of the oxygen monitor and $b_{oxygen,b}$ of the spectrometer discussed in
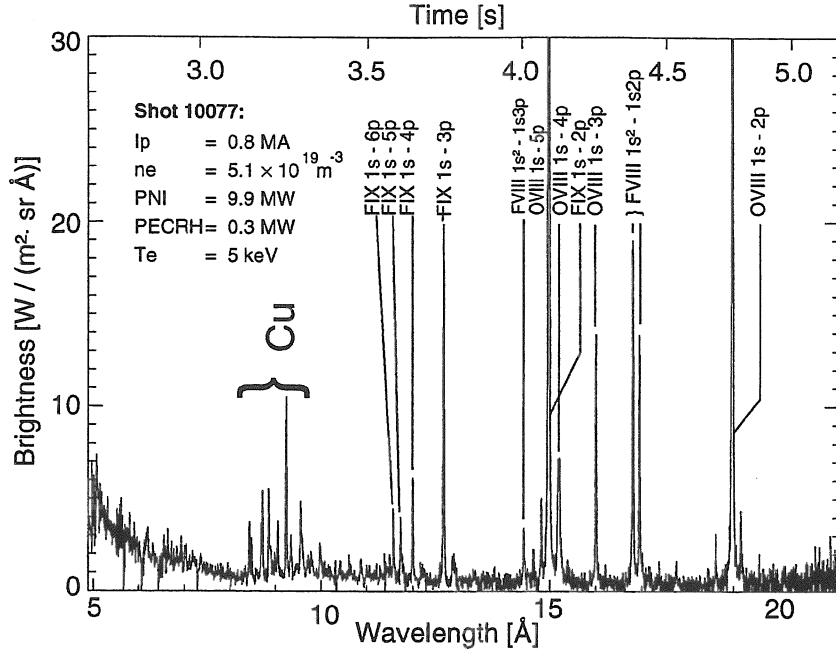
Figure 10. Typical spectrum containing the H-Like lines of F, O and also a few Cu lines after the absolute calibration

this paper:

$$\kappa = \frac{b_{\text{oxygen,a}}}{b_{\text{oxygen,b}} \cdot \gamma}. \tag{27}$$

Denoting $\rho_{\text{mylar}} = 1.38$ g/cm^3 the Mylar density, $\mu_{\text{oxy}} = \mu_{\text{mylar}}(18.97)$ Å the mass absorption coefficient of Mylar at the wavelength of the observed oxygen line, $d_{\text{nom}} = 2~\mu$m the nominal thickness of the Mylar foil the effective Mylar thickness, d_{eff} can be calculated from the correction factor κ by using

$$e^{-\rho_{\text{mylar}} \cdot \mu_{\text{oxy}} \cdot d_{\text{eff}}} = \frac{e^{-\rho_{\text{mylar}} \cdot \mu_{\text{oxy}} \cdot d_{\text{nom}}}}{\kappa} \tag{28}$$

$$\Longrightarrow d_{\text{eff}} = d_{\text{nom}} + \frac{\ln \kappa}{\rho_{\text{mylar}} \cdot \mu_{\text{oxy}}}. \tag{29}$$

The correction factor κ has been evaluated for about 30 ASDEX Upgrade discharges. Its mean value and standard deviation have been determined to be $\kappa = 0.77 \pm 0.07$ leads to an effective thickness of the mylar folie of $d_{\text{eff}} = 2.16~\mu m$, which is well inside the estimated uncertainties for the thickness. The influence of the foil thickness variation on the detector efficiency has already been shown in figure 7.

4. Results and discussion

4.1. Method of concentration measurement

Since the plasma is optically thin in the observed wavelength range, the relation between impurity concentration C at the emission zone and line intensity I for given electron density and electron temperature profiles $n_e(l)$ and $T_e(l)$ can be written as

$$C = \frac{4\pi \cdot I}{h\nu \cdot \int_l f_x(T_e(l)) \cdot n_e^2(l) \cdot \langle \sigma v_e \rangle(T_e(l)) \cdot dl}. \tag{30}$$

Here $h\nu$ denotes the energy of the emitted photons, $f_x(T_e(l))$ the fractional abundance of the observed ion and $\langle \sigma v_e \rangle(T_e(l))$ the excitation rate coefficient. Both, f_x and $\langle \sigma v_e \rangle$ are temperature dependent. $\langle \sigma v_e \rangle(T_e)$ can be determined from the ADAS database [24] whereas $f_x(T_e(l))$ must be calculated for each discharge from ionisation and recombination rates also accounting for the finite transport inside the plasma. Basically concentrations are deduced from absolute line intensity measurements by comparison with the impurity transport code STRAHL described in [23].

STRAHL needs as input parameters electron density profiles and temperature profiles. An impurity source at the plasma edge has to be adjusted in such a way that the line intensities are reproduced. From these data the impurity concentrations of all impurity ions can be calculated. For choosen emission lines with known excitation rate coefficients the line intesity can be calculated. With C_{strahl} and I_{strahl} denoting impurity concentration and emission line intensity as calculated by STRAHL the determination of impurity concentrations C_{meas} from measured line intensities I_{meas} reduce the problem of the determination of the concentration to a following equation:

$$C_{meas} = C_{strahl} \cdot \frac{I_{meas}}{I_{strahl}}. \tag{31}$$

4.2. Results

The elements nitrogen through chlor show emission lines of the H- and He-like ionisation stages within 4.5 Å and 26 Å, the usable wavelength range of the KAP crystal. With the other crystals available, which have been absolutely calibrated down to approximately 1 Å the H- and He-like ionisation stages of medium-Z elements up to Cu can be measured as well. The advantages of H- and He-like ions over ionisation stages with more electrons are the simple spectra (see figure 11) and the relatively high accuracy of atomic data available from the ADAS data base. Moreover, the He-like ionisation state owing considerably higher ionisation energies then the lower states. Therefore they exist in a relatively wide plasma temperature range. As H- and He-like copper lines are below the low wavelength limit of the KAP crystal, copper concentrations have been deduced
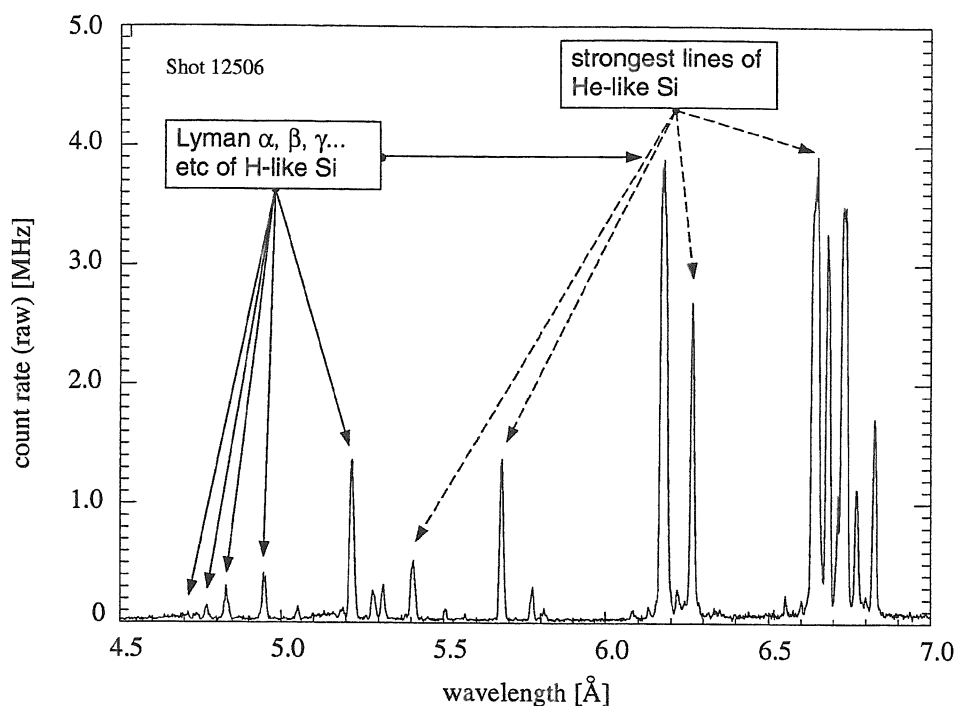
Figure 11. Spectra of H- and He-like Si measured with the Bragg spectrometer system A shortly after the siliconization of the vacuum vessel. The counter electronic is strongly saturated, therefore the intensity ratios of the consequent lines are disturbed.

from Be-like ions. By the time of these measurements the absolute calibration of the Bragg spectrometer with other crystals except KAP giving a possibility for the absolute measurements of H- and He-like copper ions was not yet available. Identification of copper against other "medium Z" elements was done by a set of Ne-like lines.

The composition of $\approx$ 2000 ASDEX Upgrade discharges has been analyzed with the result summarized in table 3. Usually oxygen and fluorine are the by far dominant impurities, followed by copper and silicon. Where the silicon originates from dust particles, which probably arise from optical fiber, sputtering of optical components and view ports. The covering the walls with silicon was time by time done in order to prevent other impurities from entering the plasma by trapping them in the wall below the Si-layer. Siliconization was performed only recently leading to much higher concentrations (up to $3 \cdot 10^{-3}$, not taken into account in this work). All other impurities occur only sporadic or have never been seen. In figure 12 the evolution of fluorine concentration with the discharge number is shown. Starting directly after a boronization the fluorine concentration first increases with discharge number and then becomes constant with a typical concentration of $\approx$ 0.15 %. Boronisation of the discharge vessel is done by

element	transition	wavelength [Å]	detection limit [ppm]	C_{meas} [ppm]		ΔZ_{eff}	
				typ.	max.	typ.	max.
N	1s – 4p	19.8	500	–	–	–	–
O	1s – 2p	19.0	19	1500	5000	0.1	0.3
F	1s – 2p	15.0	13	1500	40000	0.1	2.9
Ne	1s – 2p	12.1	8	–	–	–	–
Na	1s – 2p	10.0	< 8	–	–	–	–
Mg	1s – 2p	8.4	< 8	–	–	–	–
Al	1s – 2p	7.2	2	–	5	–	0.0008
Si*	1s – 2p	6.2	2	2	9	0.0004	0.002
P	1s – 2p	5.4	< 2	–	–	–	–
S	$1s^2$ – 1s2p	5.1	4	–	20	–	0.005
Cl	1s2p – 1s4s	19.1	3000	–	–	–	–
Cl	$1s^2$ – 1s2p	4.5	5	–	30	–	0.008
Ar	2p – 5d	13.4	1700	–	–	–	–
Ar	(1s – 2p)	(3.7)	(1)	–	(1)	–	–
Cu	$2p^2$ – 2s3p	9.2	2	10	100	0.008	0.08
Fe	1s – 2p	1.85	60	< 100	1500	< 0.1	0.3

Table 3. Composition of the ASDEX Upgrade plasma during shots 8800 – 10800. Si* - silicon concentration before the siliconization of the discharge vessel. The detection limits are given for a central electron density of $n_e = 7 \times 10^{19}$ m^{-3} and electron temperature of $T_e = 4$ keV ($\hat{=}$ 5 MW neutral injection). Fe concentration has been monitored between discharge number 12100 and 12350.

running a glow discharge in a gas mixture containing boron. This procedure builds up a boron layer on the walls of the discharge vessel, which leads to the trapping of the impurities like O and F in the wall. After a boronization the concentration is reduced to less than ≈ 0.05 %. Investigations with a teflon probe exposed to the plasma indicate that fluorine is emitted from teflon [27] by disintegration through heat and probably also by photo dissociation. About 10 monolayers of fluorine have been found on a divertor tile by PIXE [26] indicating that not all fluorine is pumped out after a plasma discharge. The remaining fluorine covers the plasma facing components as a thin layer and can be released into the next plasma discharge, therefore explaining the increase of concentration with discharge number. Immediately after a boronisation the concentration of the fluorine reaches the lowest level due to the reduction of fluorine emitting source. Then the F concentration rises systematically in the following plasma discharges in correlation

with the removal of the boron layer from the wall. With the increase of the fluorine influx from the vacuum vessel the new higher steady state concentration of fluorine is established under the assumption of a constant pumping rate of fluorine. Boronization reduces fluorine concentrations by covering the fluorine layer with boron and chemical reaction from fluorine and boron producing geseous F containing components, which are pumped off. The high fluorine concentrations which occured around discharge number 9900 were strongly reduced, after removal of some teflon containing pieces and protection of the remaining ones against direct UV- and particle flux by metal sheets. Oxygen shows the same behavior as fluorine: increasing concentrations with discharge number which are strogly decreased by boronization. Sources of oxygen are water and O_2, both being stored in the graphite tiles inside the vacuum vessel and introduced by vacuum leaks. Beside of the siliconization of the discharge vessel a possible source for silicon are dust and glass fibers contained in the vacuum vessel. Micro probe X-ray fluorescence analysis showed parts of mineral wool and other silicon containing particles in a dust sample. Dust is also a possible source for copper, as small pieces of copper cables have been found in a dust probe from ASDEX Upgrade [27].

In addition to universally present impurities like C, O, F and Si only a few other impurity species show up sporadically in some ASDEX-Upgrade plasma discharges. One of them is Fe. Iron concentrations were monitored in about 250 plasma discharges using mainly lines of He-like Fe ions at 1.85 Å. The measurements were performed in the scanning mode in the wavelength range between 1.80 Å and 1.95 Å. Up to 25 such a scans are possible during a plasma discharge. This results in a time resolution of about 0.3 s for observing the iron concentration. A continious monitoring of the Fe line intensity in maximum of the spectral line seems to be not applicable because of the strong variation of the underground signal and relatively small line intensities in this spectral range. The lines of Ne-like Fe at 17.05 Å were observed as well. They were used to determine the concentrations of Fe in some discharges applying the atom data from [28]. However these lines could rather seldom be observed as compared to He-like lines and therefore are less suitable for Fe concentration monitoring. As a result of monitoring iron was found in approximately 12 % of all discharges between 12100 and 12350. The results for the Fe concentration are also presented in Table 3. Normaly, in a typical plasma discharge done in frequently used configuration Fe can be found only in some exceptional cases as impurity events. In opposite to that, if some new plasma regimes are introduced and, hence, new parts of the wall are exposed to the plasma, strong Fe signals appear rather often. After some tens of the discharges the Fe signal goes down to the usual level namely below the sensitivity limit of the Bragg spectrometer. This suggests, that the regions of the wall, which are not directly exposed to the plasma, contain some traces of iron on the surface. So the shift of a strongly plasma exposed
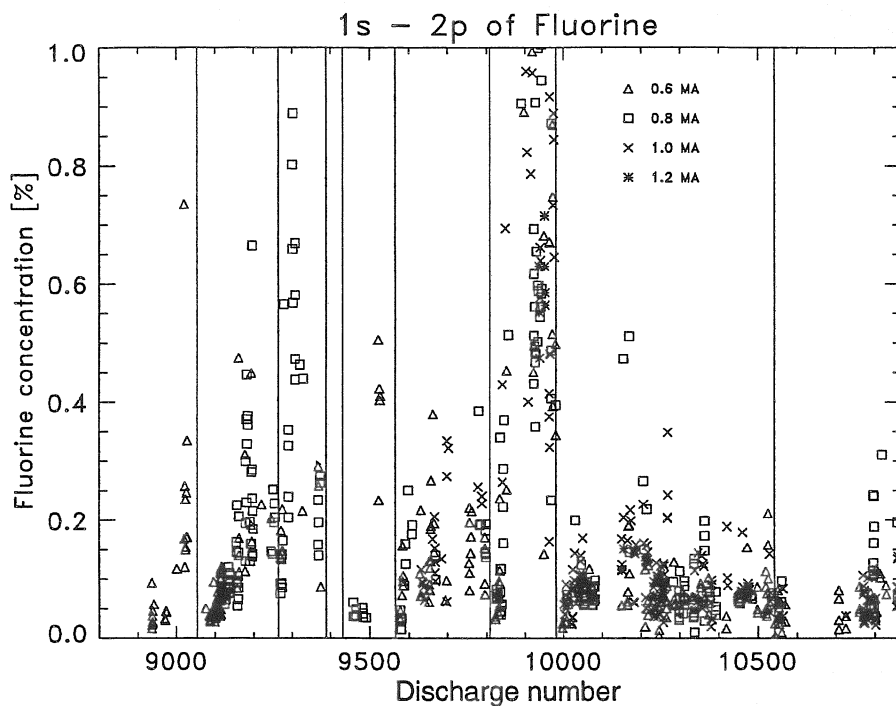
1s − 2p of Fluorine

Figure 12. Concentrations of fluorine as function of discharge number for the last ≈ 2000 ASDEX Upgrade discharges. Vertical lines indicate either boronization or vacuum vessel openings.

wall segment to the neighbouring ranges due to changing of the magnetic field configuration causes an increase of the iron influx due to errosion of the wall material. The reduction of the iron signal by further exposure of the wall to the plasma gives a hint, that impurity is contained just on the surface of the wall, and it can be removed by an erosion process and then deposed elsewhere in a deposition dominated zone of the wall.

Under the impurity species seen by the Bragg spectrometer in ASDEX Upgrade plasmas only O and F contribute substantionaly to a z_{eff} plasma radiation. The rest of the impurities stayes in most cases below the detection limit and pays almost no contribution to the plasma radiative losses. In some exception cases metallic impurities like Fe and Cu contribute to plasma radiation too.

5. Acknowledgements

[1] C. S. Pitcher and P. C. Stangeby, Plasma Phys. Control. Fusion **39** (1997) 779 – 930.

[2] J. Winter, Plasma Phys. Control. Fusion **38** (1996) 1503 – 1542.

[3] N. Peacock *et al* , "Spectroscopy for impurity control in ITER" in "Diagnostics for Experimenteal Thermonuclear Fusion Reactors (Varenna)", edited by P. Stott, G. Gorini and E. Sindoni (New York: Plenum) pp 291 - 305.

[4] R. Parker *et al* , "Plasma – wall interactions in ITER" J. Nucl. Mater. 241-243 (1997) 1-26

[5] N. J. Peacock *et al* , "Quantitative spectroscopy of x-ray lines and continua in Tokamaks", Rev. Sci. Instrum. 68(4) (1997) 1734 – 1738.

[6] M. Bessenrodt-Weberpals *et al* , Plasma Phys. Control. Fusion **38** (1996) 1543 – 1559.

[7] R. Neu *et al* , Rev. Sci. Instrum. **67** (1996) 1829.

[8] D. L. McKenzie, P. B. Landecker and J. H. Underwood, "Crystals and collimators for X-ray spectrometry", Space Science Instrumentation 2 (1976) 125 – 139.

[9] A. Oed, Nucl. Instr. Meth. **A 263** (1988) 351 – 359.

[10] A. Oed, Phys. Bl. **53** Nr. 7/8 (1997), 681 – 683.

[11] M. Oda, "High-Resolution X-Ray Collimator with broad field of View for astronomical use", Appl. Opt.4, 143,(1965)

[12] Center for x-ray optics, X-ray data booklet, ed. by D. Vaughan, PUB-490 rev., LBL, University of California Berkeley, California 94720 (1986).

[13] V. Rohde *et al* , "Comparison of boronization and siliconization in ASDEX Upgrade", Proc. 26th EPS Conf. on Contr. Fus. and Plas. Phys. Maastricht Jul. 1999, Europhysics Conference Abstracts V.23J, 1513 – 1516.

[14] K. Debertin and R. G. Helmer, "Gamma- and x-ray spectrometry with semiconductor detectors", North-Holland (1988), page 54 ff

[15] Glenn F. Knoll, "Radiation Detection and Measurement", 754 S., New York,NY: Wiley 1989, 2.Ed., pp. 96-99, ISBN: 0-471-81504-7.

[16] B. L. Henke, E. M. Gullikson and J. C. Davis, Atomic Data and Nuclear Data Tables, 54, 2 (1993), 181 – 342.

[17] Internet publication of National Institute of Standards and Technology, URL: http://physlab.nist.gov/PhysRefData/XrayMassCoef/cover.html

[18] K. D. Evans and B. Leigh, Space Science Instrumentation 2 (1976) 105 – 123

[19] B. Endras, "Aufbau und Test einer Pulshöhen-Analyse-Diagnostik für den Tokamak ASDEX Upgrade", Diploma theses, Max-Planck-Institut für Plasmapysik, Garching b. München, (1997).

[20] U. Schumacher, K. Asmussen, G. Fußmann, T. Liebsch, R. Neu "Investigation on Calibration Sources for Soft X-Ray Plasma Spectroscopy and Impurity Monitors", Rev. Sci. Instrum. **67** (1996) 2826

28

[21] R. Hall, "A Quantitative Description of Bragg Analysers", Theses submitted to the University of Leicester (1980)

[22] S. Stepanov, Computer code GID_sl_sym, http://sergey.bio.aps.anl.gov/GID_sl_sy.html

[23] K. Behringer, Internal JET Report, JET-R (87)08.

[24] Documentation available via Internet: http://patiala.phys.strath.ac.uk/adas/adas.html

[25] M. H. Chen and K. J. Reed Phys. Rev. A, **40**, 5 (1989), pp. 2292 - 2300.

[26] H. Maier, private communications.

[27] D. Bolshukhin *et al* , IPP Report, in preparation.

[28] R. Mewe, Astron. Astrophys. **20**, (1972), 215.

Geometry of signals

#13367 t=2.000

1 AUGD BLI LIHC	1
2 AUGD BLI LIHC	2
3 AUGD BLI LIHC	3
4 AUGD BLI LIHC	4
5 AUGD BLI LIHC	5
6 AUGD BLI LIHC	6
7 AUGD BLI LIHC	7
8 AUGD BLI LIHC	8
9 AUGD BLI LIHC	9
10 AUGD BLI LIHC	10
11 AUGD BLI LIHC	11
12 AUGD BLI LIHC	12
13 AUGD BLI LIHC	13
14 AUGD BLI LIHC	14
15 AUGD BLI LIHC	15
16 AUGD BLI LIHC	16
17 AUGD BLI LIHC	17
18 AUGD BLI LIHC	18
19 AUGD BLI LIHC	19
20 AUGD BLI LIHC	20
21 AUGD BLI LIHC	21
22 AUGD BLI LIHC	22
23 AUGD BLI LIHC	23
24 AUGD BLI LIHC	24
25 AUGD BLI LIHC	25
26 AUGD BLI LIHC	26
27 AUGD BLI LIHC	27
28 AUGD BLI LIHC	28
29 AUGD BLI LIHC	29
30 AUGD BLI LIHC	30
31 AUGD BLI LIHC	31
32 AUGD BLI LIHC	32
33 AUGD BLI LIHC	33
34 AUGD BLI LIHC	34
35 AUGD BLI LIHC	35
36 AUGD BLI LIHC	36
37 AUGD BLI LIHC	37
38 AUGD BLI LIHC	38
39 AUGD BLI LIHC	39
40 AUGD BLI LIHC	40

z [m]

R [m]